ADVANCED FUNCTIONAL MATERIALS
www.afm-journal.de

Defect-Driven Structural Distortions at the Surface of Relaxor Ferroelectrics

*Scarlet Kong, Nitish Kumar, Stefano Checchia, Claudio Cazorla, and John Daniels**

Relaxor-ferroelectric materials find application in a broad range of technological devices, including ultrasonic imaging transducers, nanopositioning, and high-performance capacitors. They generally exhibit occupationally disordered structures creating local polar fluctuations that are highly sensitive to applied electric or stress fields. The sensitivity of the material structure to external field and stress conditions also makes them likely to develop skin or surface phases that are unique from the bulk. Surface layers can adjust the material response and also lead to ambiguity in structural characterization. Here, using a combination of X-ray diffraction methods, it is shown that a ≈20 µm skin structure commonly exists in the lead-free relaxor-ferroelectric ceramic $(Na_{1/2}Bi_{1/2})TiO_3$–$BaTiO_3$. Using experiments and density functional theory calculations, it is shown that the combined action of oxygen vacancies providing internal chemical pressure and the surface plane stress state dictates the stability and structure of the skin layer. This work can be extended to all perovskite relaxor ferroelectrics and provides new insights into the origin of skin layers in these materials. The opportunity exists to further enhance the functionality of these materials through engineering of surface structures using the methods outlined here.

1. Introduction

Relaxor ferroelectrics are typically characterized by a broad frequency dependent peak in dielectric permittivity around the temperature of the maximum. The most technologically significant compositions have the perovskite structure with occupationally disordered cation sites. Their susceptibility to distortion under applied electric field or stress has made them ideal for high-performance electromechanical transducers, and their high dielectric constants over a broad temperature range mean they find applications in electrical capacitors.[1] Advances in the last two decades in theoretical understanding, fabrication, and characterization have led to relaxor ferroelectric being used in applications such as next generation transistors, flexoelectric devices, heterogeneous catalysis, and electrocaloric and multiferroic devices.[2] Many of these applications require the miniaturization of the functional material component, and thus the surface to volume ratio to increase significantly. This trend requires that any impact the surface volume has on the overall properties of the system be understood.

Surface layers with distinct physical properties from the bulk in thick ferroelectric materials have been observed since the 1950s.[3] There are several reports showing discrete surface layers in $BiFeO_3$ and even nonferroelectrics such as $SrTiO_3$ and disordered yttria-stabilized zirconia.[4] In some cases, the skin structure is quite thin (≤1 µm). For example, in $BiFeO_3$, a skin structure with an elongated out-of-plane lattice parameter was observed to extend only for a few nanometers from the surface.[4c] An anomalous surface layer or "skin" has been previously studied in lead-based relaxor ferroelectrics, as it caused long-lasting ambiguity in the phase identification of these systems.[5] For a single crystal of relaxor $Pb(Zn_{1/3}Nb_{2/3})O_3$ (PZN), using X-ray diffraction (XRD) with different X-ray energies and thus penetration depths, a skin layer of ≈10–50 µm showed a shoulder within the diffraction pattern next to the parent peak (or simply referred to as "shoulder" henceforth), while the bulk of the sample had a single symmetric peak representing a cubic structure.[6] Similarly, $Pb(Mg_{1/3}Nb_{2/3})O_3$ (PMN), PZN–$PbTiO_3$ (PZN–PT), and PMN–PT are also known to exhibit a skin structure.[7] There are other interesting reports on the skin structures in Pb-based relaxors. For example, it was reported that the shoulders did not appear on freshly fractured surfaces, but they appeared once the surface was polished.[7a,b] The intensity of the shoulders was shown to depend on the particle size of the polishing media, with larger particle sizes resulting in more pronounced shoulders. The existence of the skin has been challenged in some studies too. Using neutron time-of-flight measurements undertaken in transmission mode on powder and single crystals of unpoled PZN samples, it was found that the overall structure was rhombohedral, in contradiction to cubic bulk symmetry reported by other researchers.[8]

Even though there is a wealth of observations of skin structures in lead-based relaxor ferroelectrics, their mechanisms of

S. Kong, Dr. N. Kumar, Dr. C. Cazorla, Dr. J. Daniels
School of Materials Science and Engineering
Faculty of Science
University of New South Wales
Sydney, NSW 2052, Australia
E-mail: j.daniels@unsw.edu.au
Dr. S. Checchia
European Synchrotron Radiation Facility (ESRF)
Grenoble 38000, France
The ORCID identification number(s) for the author(s) of this article can be found under https://doi.org/10.1002/adfm.201900344.

DOI: 10.1002/adfm.201900344

formation remain elusive. There have been several attempts to comprehend this phenomenon. It was suggested that this skin structure may originate due to random electric fields present in the relaxors resulting from the presence of multiple cations with different valence sharing a sublattice position.[4i] This idea was first proposed by Stock et al. and Cowley et al. due to a similar skin effect exhibited by random-field Ising antiferromagnet materials such as $Mn_{1/2}Zn_{1/2}F_2$.[5a,9] Gao et al. argued that skin structure may be a result of bound charges induced by subsurface polarization, which should be screened by structural distortions, redistribution of charge carriers, or electronic reconstruction.[10] Another study attributed the presence of the skin to compositional differences between the surface and bulk (e.g., clustering of magnesium at the surface for PMN), which leads to changes in the unit cell and strain.[11]

Apart from enhancing the understanding of structure, which is central to ferroelectrics research, the skin can also impact macroscopic properties, such as the flexoelectric effect (coupling between polarization and strain gradients). It has been reported that a large flexoelectric effect originates in unpoled $BaTiO_3$ ceramics due to the presence of a several micrometers thick spontaneously polarized skin, which can be sustained even above the Curie point.[12] Similarly, skin structure may also be responsible for the large flexoelectric effect reported in $(Ba_{1-x}Sr_x)TiO_3$ (BST).[13] Skin structures have also been suggested to contribute to large low-frequency polarization noise observed in common relaxor ferroelectrics, having the potential to degrade the performance of sensitive acoustic transducers.[14] Skin structures may also have the potential to be functionalized in applications in future transistor technology,[15] voltage-controlled catalysis,[16] and spintronics.[4c]

Here, we report the presence of a skin structure in $(Na_{1/2}Bi_{1/2})TiO_3$–$BaTiO_3$ (NBT–BT) relaxor ferroelectric ceramics. The NBT-based ceramics have received significant attention from the research community due to their potential to replace Pb-based ceramics in piezoelectric devices, and applications in high temperature capacitors and solid oxide fuel cells.[17] There are several articles that summarize the structural, electrical, and transport properties of NBT–BT.[17b,18] Similar to the situation that occurred in their Pb-based counterparts, the formation of a unique skin structure has likely contributed to the ambiguity in structural characterization of NBT-based ceramics, as different measurement methods have different sensitivities to the surface or bulk structures.[19] We show that this skin structure in NBT–BT is intimately related to the underlying defect chemistry and point defect concentration, particularly oxygen vacancies, and their interaction with the surface stress state. By altering the oxygen vacancy concentration, this skin structure can be altered. This is supported by density functional theory (DFT) calculations which show that oxygen vacancies can provide the driving force for this skin structure formation.

2. Results and Discussion

Figure 1 demonstrates the existence of a skin structure in NBT–BT by comparing diffraction patterns obtained from laboratory and synchrotron X-ray sources. The penetration depth of the laboratory CuKα X-rays into the surface of the ceramic was calculated to range between 4.5 and 11 µm for a Q value range of 1.60–3.95 Å^{-1}. This was calculated using absorption values of the constituent elements, sample density, and incident angle.[20] The synchrotron pattern was measured in transmission geometry using high energy X-rays and sampled the center of the bulk ceramic. The synchrotron pattern exhibits a macroscopic cubic symmetry in Figure 1b, which is typical of NBT–BT relaxors without a long-range ordered structure.[21] In contrast, shoulders (indicated by black arrows in Figure 1a) are observed for laboratory XRD pattern. This demonstrates that the structural distortion that gives rise to these shoulders is limited to the surface of the ceramic.

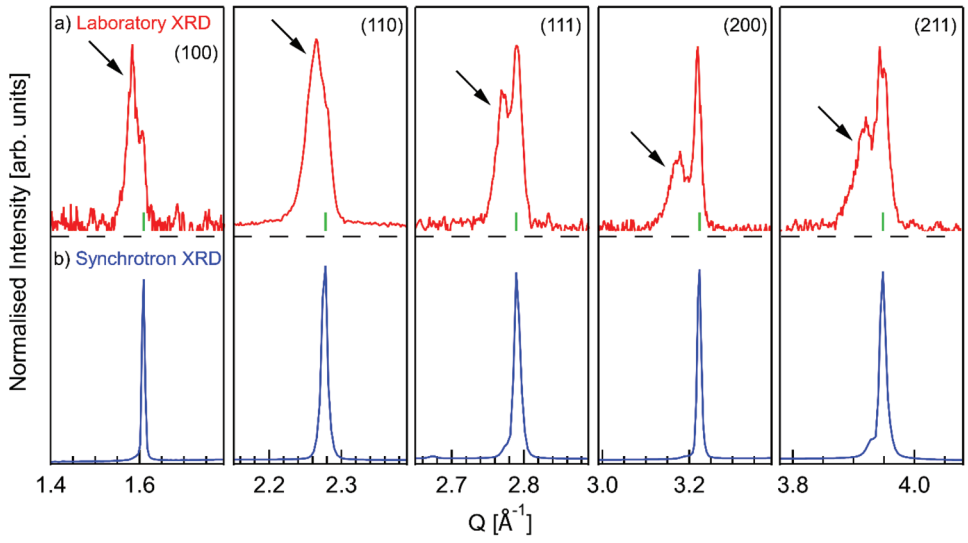

Figure 1. Reflection geometry laboratory XRD performed on ceramic surface a) compared with transmission geometry synchrotron XRD from the bulk b). The low-angle shoulders have been indicated with black arrows. It can clearly be seen than the shoulders are only prominent for laboratory XRD data. The positions of parent peaks have been shown with vertical green markers.

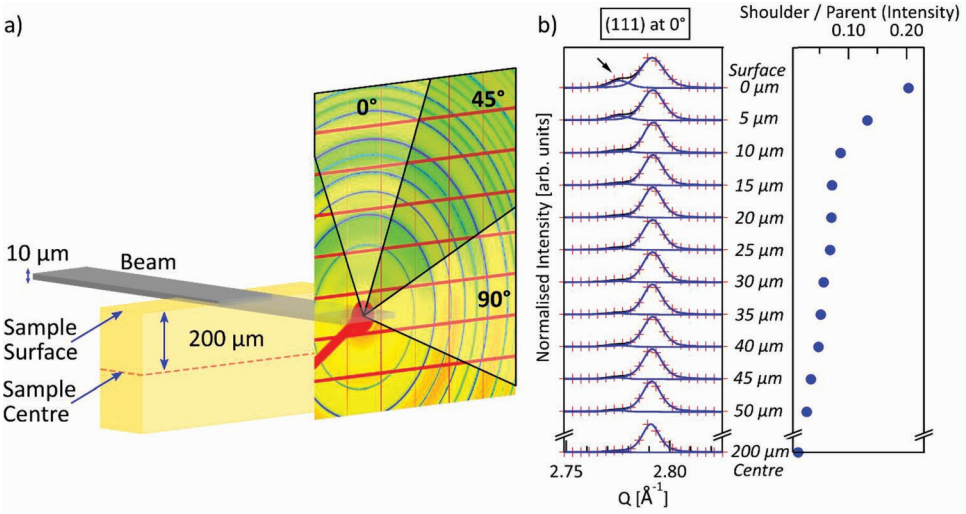

Figure 2. A schematic of the setup used for scanning diffraction patterns from surface to center of the ceramic using a 10 µm beam height a). The angles in the schematic's 2D synchrotron diffraction patterns represent the angles between surface normal and **q**-vector. The depth profile for (111) peak from the surface to the sample center is shown in (b). The low-angle shoulder at the surface has been indicated with a black arrow. Corresponding ratios of integrated intensities of shoulders to parent peak are also shown. It is apparent that the shoulders significantly reduce in intensity on moving toward the center of the ceramic.

The appearance of these shoulders on the low-angle (or low-*Q*) side of the bulk phase indicates that this skin structure has a larger *d*-spacing than the parent structure. This is different from several reports on Pb-based relaxors such as PZN and PZT–PT, where the skin has a slightly smaller (≈0.2%) lattice parameter than the bulk.[5b,22] It should also be noted that the shoulders in Figure 1 do not originate due to a secondary cubic phase with a larger lattice parameter, as a single lattice parameter cannot estimate all peak positions correctly. Also, this skin structure persisted irrespective of the amount of surface removal performed on the sample. We tested the samples ground by different amounts (100–1000 µm) and in different mediums (dry, water, or ethanol), and all of them showed an identical skin structure. This suggests that the skin was not a consequence of difference in chemical composition between the bulk and the surface.

To measure more accurately the thickness of the skin, a 10 µm synchrotron X-ray beam was scanned from the surface to the sample center (200 µm deep from surface) in 5 µm steps, as shown in **Figure 2**a. The (111) peaks for each beam position and the corresponding ratios of integrated intensities of the shoulder to parent peak (Figure 2b) are also shown. It can be seen that the shoulders are most intense at the surface and the ratio of integrated intensities diminishes quickly and stabilizes at a depth of ≈20 µm.

Figure 3 shows the (111) peaks measured at different angles between surface normal and the scattering vector. This is obtained by integrating different azimuthal regions of a 2D diffraction pattern as indicated in the schematic diagram (Figure 2a). This method is used for investigating preferred orientation or texture in a sample. An ≈90% decrease in the ratio of the shoulder to parent integrated intensities (from 0.29 to 0.03) is observed for the (111) as the lattice planes under investigation move from parallel (0° angle in Figure 3a)

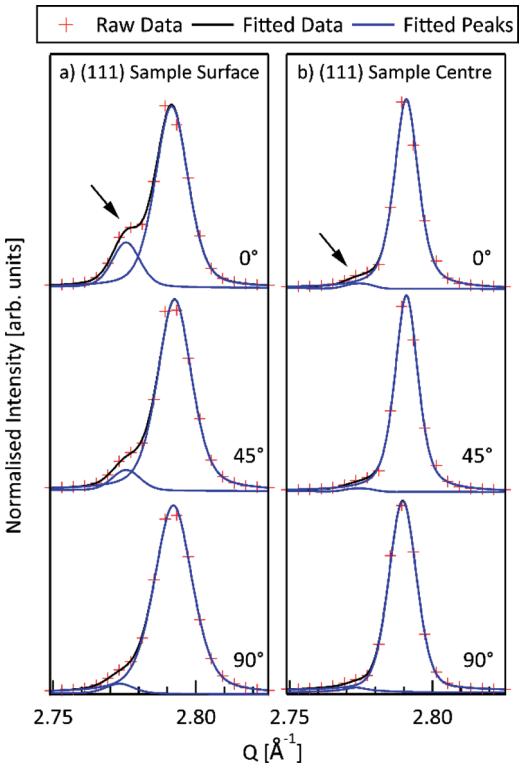

Figure 3. (a) and (b) show the orientation dependence of the intensity of shoulders at the sample surface (beam center at 0 µm from surface) and sample center (200 µm from surface), respectively, using the (111) peak. The orientation dependence is obtained from 2D synchrotron diffraction patterns as indicated in Figure 2a. The low-angle shoulder peaks are indicated with black arrows. The angles mentioned are between the surface normal and diffraction scattering vector. It is apparent that there is a preferred orientation at the surface, but not in the center.

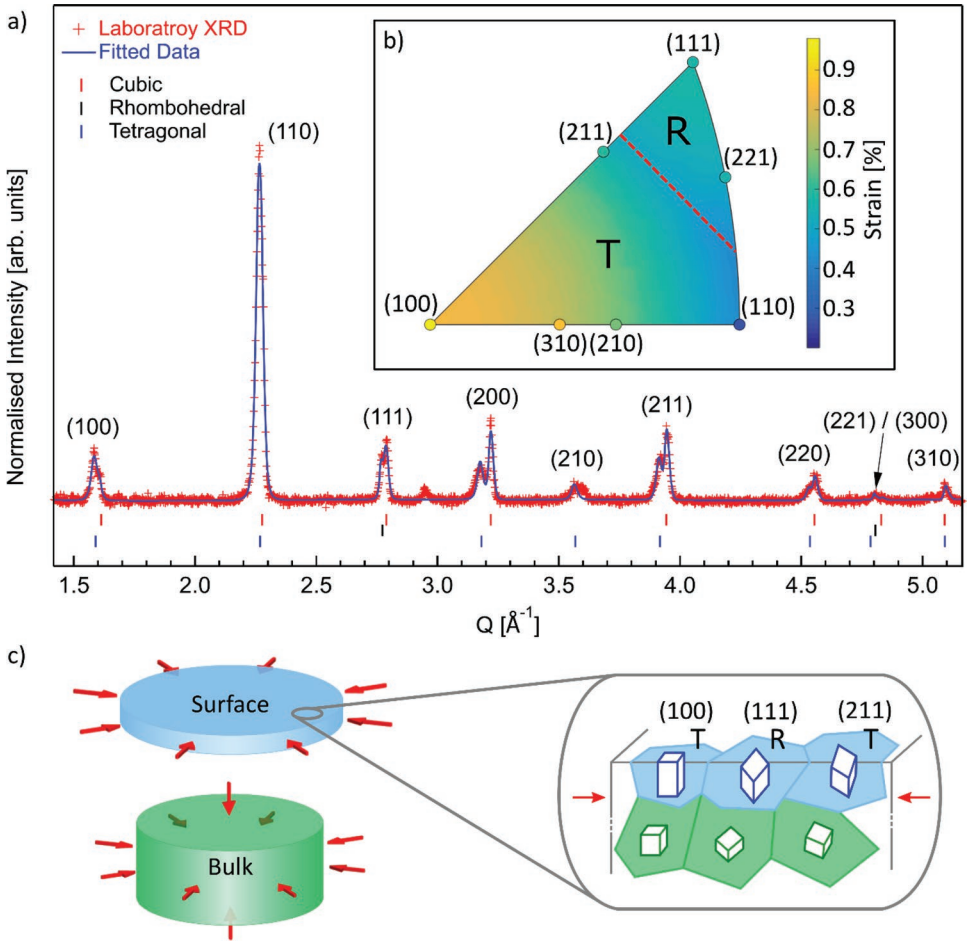

Figure 4. a) Laboratory XRD collected with the scattering vector, **q**, perpendicular to the sample surface. Fitted curves showing the parent cubic phase and tetragonal or rhombohedral peaks fitting the low-angle shoulders. b) Strain for given grain orientations calculated from the fitted peaks, plotted on an inverse pole figure (strain magnitude given in the color scale). Two phase regions are marked for given grain orientations. c) A simplified schematic comparing the stress states in the skin surface (blue) and bulk (green). While a biaxial stress state exists at the surface and the material is free to expand in the direction perpendicular to the surface, allowing any distortions to occur (as shown by the blue grains), a triaxial stress state is experienced in the bulk of the ceramic. The right schematic shows that grains with different orientations are present in the skin and expand along the surface normal.

to perpendicular (90° angle in Figure 3a) to the sample surface. This indicates a skin structure for which the distortion from the parent structure is anisotropic and textured about the sample surface normal. This implies the crystal structure is preferentially elongated out-of-plane at the surface. The shoulders measured at the sample center (Figure 3b), on the other hand, are visibly smaller than the surface and isotropic without any orientation dependence.

The existence of a skin structure and its textured nature are suggested to be a result of the different stress conditions at the surface as compared to the bulk. It is known that the surface exists under a biaxial stress condition (plane stress), with no constraint present normal to the surface. On the other hand, the bulk of the sample is expected to be triaxially constrained under plane strain condition.[23] This is illustrated in **Figure** 4c. At the surface, any strain introduced in the lattice can be relieved by a lattice expansion (or contraction) along the direction of the surface normal (but not radially). In polycrystalline samples, since the skin has grains with different orientations intersecting it, a unique distortion and texture exist for all the peaks in the diffraction pattern. As has been previously observed, NBT–BT compositions in the MPB can undergo both field and stress induced transformations to rhombohedral and/or tetragonal symmetries.[24] This mixed phase transformation has been suggested to be grain orientation dependent, allowing large strains in bulk polycrystals.[25] Thus, the skin structure observed in NBT–BT exhibits a distortion similar to the mixed phase transformation described by Oddershede et al.[25]

Figure 4a shows laboratory XRD data fit with three phases. First, the cubic ($Pm\bar{3}m$) structure is used to fit the bulk phase. Then, tetragonal ($P4mm$) and rhombohedral ($R3c$) phases are added. However, only the peaks expected to provide the maximum ferroelastic strain out-of-plane for a given reflection are nonzero intensity. In this case, the shoulder peak on the (100) is fit with a (001) tetragonal peak. The shoulder of the (111) peak is fit with rhombohedral (202) (that is (111) in the parent cubic cell setting). Figure 4b shows an inverse pole figure which allows us to assign the shoulder peak of each reflection to a given symmetry. A marker is placed on the inverse pole figure for each reflection. This represents a given grain

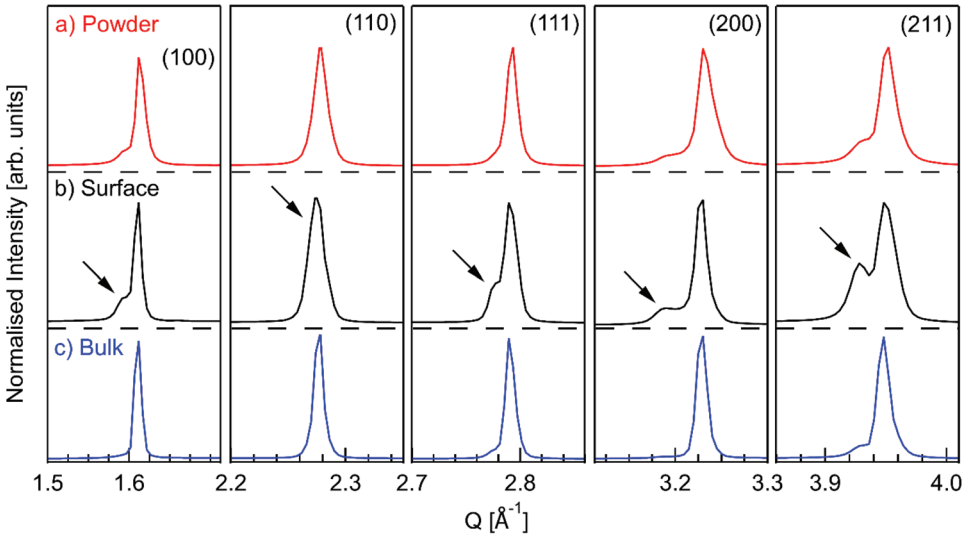

Figure 5. Synchrotron diffraction pattern of crushed ceramic powder a) compared with surface b) and bulk c) of a ceramic pellet. The shoulders have been indicated by black arrows for the ceramic surface. It can be seen that on crushing the ceramics to powders, the shoulders become weaker and appear similar to bulk.

orientation relative to the sample surface, as shown in the schematic Figure 4c. The color scale on Figure 4b represents the strain magnitude between the shoulder peak and the parent peak for each grain orientation. All grain orientations to the bottom left of the dashed red line in the inverse pole figure are expected to have a tetragonal symmetry, while those to the top right are expected to have rhombohedral symmetry.

It is shown how the strain magnitude of the shoulder position varies according to the grain orientation measured. On initial observation of the diffraction patterns, it appears as though the (110) peak has no shoulder, however, this is explained by the analysis provided. For both tetragonal and rhombohedral distortions of the surface grains, the maximum ferroelastic strain for the (110) is only ≈0.2%. Thus, the shoulder of the (110) peak cannot be resolved from its parent cubic peak and appears single. Interestingly, this analysis shows that if a single crystal with the same surface structure was observed on the 111 face, a rhombohedral structure would be seen, while if observed on a 100 face, a tetragonal structure would be observed. This effect is likely also occurring in lead-based relaxor single crystals, and may be an additional complication to the correct characterization of the skin layers.

Using the reported mechanical properties of K_{1C} = 1.1 MPa $\sqrt{\text{m}}$ and transformation stress of 344 MPa for NBT–BT,[26] the surface thickness that exists in a plane stress condition is calculated to be 3.2 µm. Beyond a depth of 25 µm, NBT–BT should be under a plane strain condition.[26] Between 3.2 and 25 µm, it should exhibit a transition region from plane stress to plane strain. These values are consistent with our results shown in Figures 2 and 3, where the intensity of the shoulders appears to reach a consistent minimum at a depth of ≈20 µm. The remaining shoulder peak intensities in the bulk of the material show no preferred orientation with respect to any sample direction. It is likely that these distortions, which are of much lower volume fraction than the surface, may be related to free surfaces in the bulk of the material, such as those at pores.

To further demonstrate that the textured skin layer is only present in a ceramic material where a plane stress state exists at the surface, **Figure 5**a shows the diffraction pattern measured from a crushed powder of the same material. It can be seen that the shoulders for powders have much lower intensity as compared to skin (Figure 5b), and are comparable to the center or bulk (Figure 5c) of the ceramic. This change in diffraction profile between a powder and ceramic specimen further contributes to the structural ambiguity reported in these systems.

Figures 1–5 above provide clear evidence of the presence of a textured skin structure in NBT–BT ceramics and showed this is related to the plane stress condition at the ceramic surface. In the following sections, we will show that internal chemical pressure, originating due to defect equilibrium concentrations, acts as a driving force to distort the lattice and is intimately related to this observed skin structure.

Oxygen vacancies are known to be a source of internal chemical pressure and alter the lattice parameters in ceramic oxide materials. For example, in $SrTiO_3$, diffusion of oxygen vacancies to the surface along preferred directions on application of an electric field causes a reversible appearance of a skin structure.[27] In thin films such as $BaTiO_3$, an increase in the concentration of oxygen vacancies results in larger lattice parameters.[28] Lattice parameter expansion (or contraction) due to internal chemical pressure caused by oxygen vacancies has been extensively studied in materials for electrolyte applications, such as solid oxide fuel cells.[29] The atomic phenomenon leading to this internal chemical pressure is not completely established, however, it is argued to be a result of three major factors in the case of fluorite structured ceramics (e.g., ZrO_2 or CeO_2): 1) electrostatic repulsion between cations surrounding the oxygen vacancy, 2) increase in the ionic radius of a reducible cation (e.g., Ti^{4+} to Ti^{3+}) in the case of charge compensation of oxygen vacancies by Ti^{3+} defects, and 3) lower effective ionic radius of an oxygen vacancy (calculated by assuming no change in cation radii on introducing an oxygen vacancy) due to

oxygen anions moving closer to each other. A superposition of these factors can determine the magnitude of lattice expansion (or contraction) on changing oxygen vacancy concentration.[30]

In the case of fluorites, internal chemical pressure due to oxygen vacancies has always been observed to result in lattice expansion.[29] However, the effective ionic radius of an oxygen vacancy was computed to be lower for fluorites (e.g., 1.17 Å for CeO_2) than the oxygen ion itself (1.38 Å). Therefore, it was suggested that the first two factors mentioned above dominate the third for fluorites. In contrast, for perovskites, the effective oxygen vacancy radii were shown to be larger (1.24–1.57 Å) than fluorites, with some of them even larger than the oxygen anion (1.40 Å).[29] Our DFT calculations estimated the effective ionic radius of an oxygen vacancy in NBT to be 1.515 Å, which is larger than the oxygen anion. This suggests that chemical pressure due to oxygen vacancies is likely to result in a lattice expansion in NBT-based ceramics, as per the three factors mentioned above.

To experimentally demonstrate the role of oxygen vacancies and show that the skin structure in NBT–BT is directly related to oxygen vacancy concentration, we intentionally altered the defect concentration of the material. Previous reports have shown that the NBT-based and other bismuth-containing systems naturally have significant concentrations of cation vacancies and anion vacancies, which are the result of volatile cations, high temperature processing conditions, hygroscopic precursors, and entropy requirements.[17b,31] A generic charge neutrality condition in Kröger–Vink notation can be written as in Equation (1)

$$[V'_{Na}] + 3[V'''_{Bi}] + n + [A'] \approx p + 2[V^{\bullet\bullet}_{O}] \quad (1)$$

where, n and p are electron and hole concentrations, and V'_{Na}, V'''_{Bi}, A' and $V^{\bullet\bullet}_{O}$ are sodium vacancy, bismuth vacancy, unavoidable acceptors associated with precursor powders, and oxygen vacancies, respectively.[32] The nonstoichiometry was introduced in our ceramics by adding 2 mol% more bismuth (BiXs) or less bismuth (BiDef) than the stoichiometric amount during the initial processing step. These ceramics were subsequently sintered in air. It is well-documented that for NBT-based systems the ionic compensation mechanism is dominant at oxygen partial pressures close to air.[17b,c,33] This has in fact been utilized to achieve excellent oxygen ion conduction in these systems.[17b] An increase in bismuth vacancy concentration (e.g., in BiDef), therefore, is expected to increase the oxygen vacancy concentration as per the Equation (1) above and defect incorporation reaction in Equation (2)

$$\text{BiDef:}\quad 2Bi^{x}_{Bi} + 3O^{x}_{O} - Bi_2O_3 \rightarrow 2V'''_{Bi} + 3V^{\bullet\bullet}_{O} \quad (2)$$

Similarly, in BiXs samples, the oxygen vacancy concentration is expected to be significantly lower than a stoichiometric sample due to reduced concentration of V'''_{Bi} (Equation (3)) and potential formation of positively charged defects such as $Bi^{\bullet\bullet}_{Na}$ (Equation (4)), as also shown in a previous study.[34] Our DFT calculations showed that the introduction of only V'''_{Bi} in bulk NBT results in a small volume contraction by 0.06% as compared to the stoichiometric system. Meanwhile, introduction of only $V^{\bullet\bullet}_{O}$ leads to a moderate volume expansion by 0.46%. The net result of introducing both V'''_{Bi} and $V^{\bullet\bullet}_{O}$ in bulk NBT therefore should be an expansion of the system. Thus, $V^{\bullet\bullet}_{O}$ along with compensating V'''_{Bi} can be a source of net positive internal chemical pressure in NBT–BT ceramics. This internal chemical pressure combined with plane stress condition at the surface is proposed to increase the thickness of the textured skin structure

$$\text{BiXs:}\quad 3V^{\bullet\bullet}_{O} + 2V'''_{Bi} + Bi_2O_3 \rightarrow 2Bi^{x}_{Bi} + 3O^{x}_{O} \quad (3)$$

$$\text{BiXs:}\quad 3V^{\bullet\bullet}_{O} + 6V'_{Na} + Bi_2O_3 \rightarrow 2Bi^{\bullet\bullet}_{Na} + 3O^{x}_{O} + 4V'_{Na} \quad (4)$$

The XRD patterns taken from the surface layer of stoichiometric, BiDef, and BiXs samples are compared in **Figure 6**. It is clear that the BiDef sample, which has a higher concentration of V'''_{Bi} and $V^{\bullet\bullet}_{O}$, has a larger shoulder peak suggesting a more significant skin layer. The shoulder peaks for BiXs sample, on the other hand, are not visible. This supports the hypothesis that the skin structure is dependent on oxygen vacancy concentration, which can be altered to decrease or increase the internal chemical pressure. Similar to Figure 1, shoulders on the lower-angle sides of parent peaks suggest that the overall effect of oxygen vacancies is an expansion rather than contraction of the unit cell within the skin layer, which is consistent with our DFT results.

An additional experiment to demonstrate that the skin structure is influenced by the oxygen vacancy concentration, and to further eliminate the possibility of mechanical influence, was performed by annealing a stoichiometric NBT–BT sample in oxygen, air, and then nitrogen at 600 °C for 10 h. This temperature has been demonstrated to be sufficient to alter the oxygen vacancy concentration at the surface.[17b,35] Annealing in nitrogen, which has a lower oxygen partial pressure than air, is expected to increase the oxygen vacancy concentration, while annealing in oxygen is expected to have the opposite effect. Using the known diffusion rate in related materials, these treatments are expected to alter the oxygen concentration within approximately the first 40 µm of material.[17b] XRD (**Figure 7**) was performed after each annealing stage using a laboratory diffractometer, which has been shown to be sensitive to the skin structure. It can be seen that the shoulder peaks were significantly reduced in size for the sample annealed in oxygen, consistent with results in Figure 5. Annealing the sample in air at 600 °C had no visible effect on the intensity of the shoulders as compared to Figure 1, suggesting that this skin structure is thermally stable.

It should be noted that, in addition to the oxygen vacancies, the chemical pressure from the barium cation, which is larger in size than sodium or bismuth,[36] could also contribute to the internal chemical pressure leading to a skin structure. However, studying the effect of barium nonstoichiometry independently may be challenging, as it is also expected to alter oxygen nonstoichiometry due to charge-neutrality conditions. Finally, a well-understood skin structure, its relationship to the underlying defect chemistry, and its potential application to functional phenomena (e.g., flexoelectricity) effect makes this study important for the ferroelectrics research community.

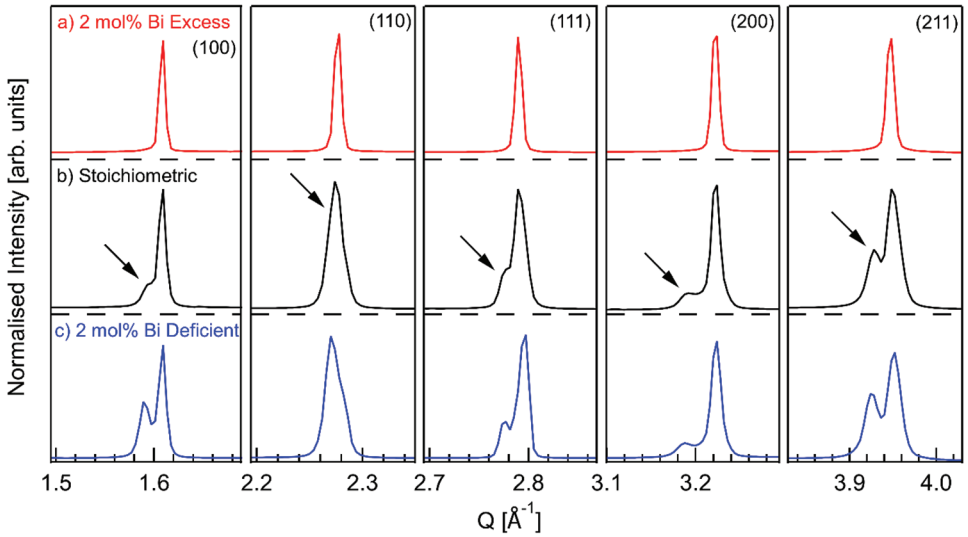

Figure 6. Synchrotron diffraction patterns from the surface for nonstoichiometric samples, BiXs a) and BiDef c), compared with stoichiometric sample b). The shoulders have been indicated by black arrows for the stoichiometric sample. It can be seen that for the sample with deficient bismuth content (or higher oxygen vacancy concentration), the shoulders become more prominent, while they were removed entirely for the sample with excess bismuth content (or lower oxygen vacancy concentration).

3. Conclusions

This work showed that an ≈20 µm skin structure exists in $(Na_{1/2}Bi_{1/2})TiO_3$–$BaTiO_3$ relaxor ceramics, and is a consequence of two factors: 1) a plane-stress condition at the surface and 2) oxygen vacancies, which apply internal chemical pressure to the system. The skin structure is elongated out-of-plane, with individual grains possessing a given symmetry based on their orientation relationship to the surface normal. It was demonstrated that the texture does not exist for powders, and the intensity (or volume fraction) of the surface structure peaks are reduced in the state to which the plane stress condition does not apply. The role of oxygen vacancies has been investigated by intentionally altering their concentration using nonstoichiometry and annealing under different oxygen partial pressures. Using DFT, it was shown that oxygen vacancies apply an internal chemical pressure acting to expand the unit cell, thus, that the skin structure peak intensities were proportional to oxygen vacancy concentration. These results provide not only important insights toward answering the long-standing question of the origin of skin structures in relaxor ferroelectrics, but also mechanisms to control their

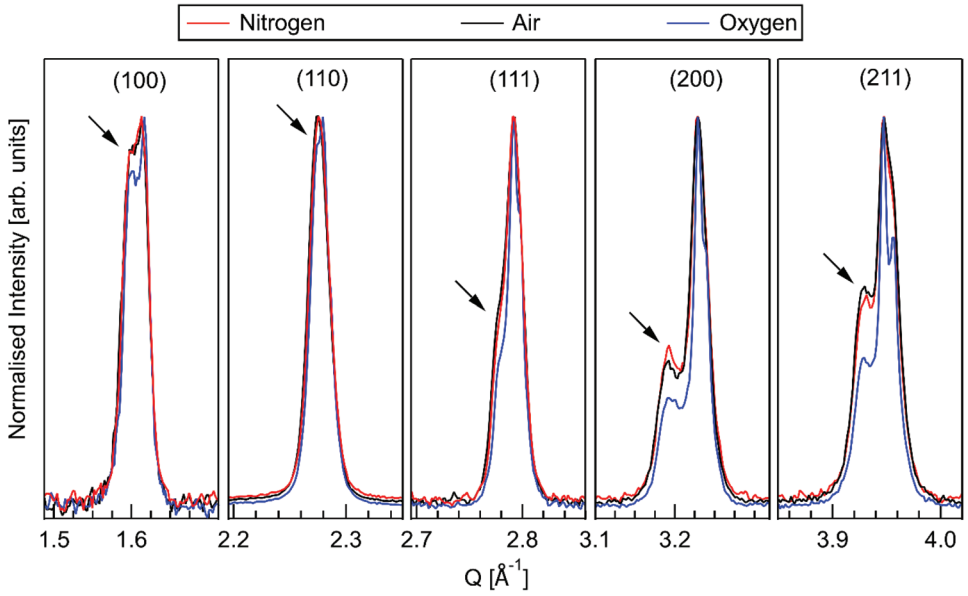

Figure 7. Surface diffraction patterns of a stoichiometric sample annealed in nitrogen, air, and oxygen at 600 °C for 10 h. The shoulders have been indicated by black arrows. It can be seen that for the sample annealed in oxygen, the shoulder peak intensity is reduced.

formation for potential investigations aiming to functionalize them.

4. Experimental Section

Stoichiometric and nonstoichiometric NBT–6BT were synthesized using the conventional solid-state oxide method, as described elsewhere.[34] NBT–BT is known to exist in the morphotropic phase boundary region, in the nonergodic relaxor state, possessing long-range cubic symmetry prior to the application of electric field or stress.[37] XRD measurements were conducted using both laboratory and synchrotron X-ray sources. In both diffraction measurements, the surfaces of the samples were ground to ≈2.5 µm finish. For measurements on powdered material, sections of the same pellets were crushed using a mortar and pestle, giving an expected particle size between 1 and 10 µm. Laboratory XRD was performed on a PANalytical Xpert Multipurpose X-ray Diffraction (MPD) system using CuKα radiation in reflection geometry. High energy X-ray measurements were performed at the European Synchrotron (ESRF), beamline ID15A, in transmission geometry with a beam energy of 65 keV. The beam geometry could be adjusted to achieve a narrow vertical beam size. This was measured directly using an imaging camera in the sample position and had a resultant full width at half maximum of ≈10 µm. A schematic of the synchrotron XRD setup is shown in Figure 2. In this case, the beam position within the sample was adjusted in order to sample successive layers from the surface to the bulk. A large area detector was used to collect the diffraction information in the forward geometry.[38] Angular dispersive diffraction profiles were obtained through radial integration of the diffraction images. Peak fits were performed using a pseudo-Voigt function. Texture measurements were taken using synchrotron XRD where the raw 2D diffraction images were integrated over 45° azimuthal ranges (as indicated in Figure 2).

Energetic and structural properties of bulk (1–x)NBT–xBT (x = 0.0% and 12.5%) were estimated with first-principles methods based on density functional theory. The Perdew–Burke–Ernzerhof variant of the generalized gradient approximation to DFT[39] was used as is implemented in the VASP package.[40] The "projector augmented wave" method was employed to represent the ionic cores,[41] and the following electrons were considered as valence: Na's 3s and 2p; Bi's 5d, 6s, and 6p; Ti's 3p, 4s, and 3d; Ba's 5s, 5p, and 6s; O's 2s and 2p. Wave functions were represented in a plane-wave basis truncated at 650 eV, and a 40-atom simulation cell was used that allowed to reproduce the usual phases appearing in relaxor ferroelectrics.[42] For integrations within the first Brillouin zone, a Gamma-centered k-point grid of $6 \times 6 \times 6$ was adopted. Geometry relaxations were performed by using a conjugate-gradient algorithm that changed the volume and shape of the unit cell. The imposed tolerance on the atomic forces was of 0.01 eV Å^{-1}. By using these parameters, total energies were obtained that converged to within 0.5 meV per formula unit (f.u.). The calculation of the "effective ionic radius for an oxygen vacancy"[29b] in NBT was performed by removing two electrons along with an oxygen atom from the system. A pseudocubic crystal symmetry was imposed in all the calculations.

Acknowledgements

S.K. and N.K. contributed equally to this work. J.D. and C.C. acknowledge support from the Australian Research Council's Discovery Project and Future Fellowship funding schemes (project numbers DP130100415 and FT140100135). S.K. acknowledges funding from the Australian Institute of Nuclear Science and Engineering Honours Scholarship Program. The European Synchrotron is acknowledged for the provision of experimental beamtime. Computational resources and technical assistance were provided by the Australian Government and the Government of Western Australia through Magnus under the National Computational Merit Allocation Scheme and The Pawsey Supercomputing Centre.

Conflict of Interest

J.D. is director of Critus Pty. Ltd.

Keywords

defect chemistry, DFT, diffraction, relaxor ferroelectric, skin structure

Received: January 11, 2019
Revised: April 2, 2019
Published online:

[1] a) W. Heywang, K. Lubitz, W. Wersing, *Piezoelectricity: Evolution and Future of a Technology*, Springer Science & Business Media, New York, NY **2008**; b) B. Jaffe, *Piezoelectric Ceramics*, Elsevier, London **2012**; c) Y. Xu, in *Ferroelectric Materials and Their Applications* (Ed: Y. Xu), Elsevier, Amsterdam **1991**, p. 1.

[2] a) N. Setter, D. Damjanovic, L. Eng, G. Fox, S. Gevorgian, S. Hong, A. Kingon, H. Kohlstedt, N. Park, G. Stephenson, *J. Appl. Phys.* **2006**, *100*, 051606; b) L. W. Martin, A. M. Rappe, *Nat. Rev. Mater.* **2017**, *2*, 16087.

[3] a) P. Coufova, H. Arend, *Cechoslovackij Fiziceskij Z. B* **1960**, *10*, 663; b) P. Coufova, H. Arend, *Cechoslovackij Fiziceskij Z. B* **1962**, *12*, 308; c) N. Setter, E. Colla, *Ferroelectric Ceramics: Tutorial Reviews, Theory, Processing, and Applications*, Birkhauser, Basel, **1993**; d) U. Höchli, H. Rohrer, *Phys. Rev. Lett.* **1982**, *48*, 188; e) A. Radni, X. Gerbaux, *Croat. Chem. Acta* **1988**, *61*, 671.

[4] a) G. Shirane, R. Cowley, M. Matsuda, S. Shapiro, *Phys. Rev. B* **1993**, *48*, 15595; b) U. Rütt, A. Diederichs, J. Schneider, G. Shirane, *Europhys. Lett.* **1997**, *39*, 395; c) X. Martí, P. Ferrer, J. Herrero-Albillos, J. Narvaez, V. Holy, N. Barrett, M. Alexe, G. Catalan, *Phys. Rev. Lett.* **2011**, *106*, 236101; d) J. Kondoh, *J. Alloys Compd.* **2004**, *375*, 270; e) Y. Kitano, Y. Mori, A. Ishitani, T. Masaki, *J. Am. Ceram. Soc.* **1988**, *71*, C-34; f) J. J. Roa, M. Turon-Vinas, M. Anglada, *J. Eur. Ceram. Soc.* **2016**, *36*, 1519; g) T. Thurston, G. Helgesen, D. Gibbs, J. Hill, B. Gaulin, G. Shirane, *Phys. Rev. Lett.* **1993**, *70*, 3151; h) P. Gehring, K. Hirota, C. Majkrzak, G. Shirane, *Phys. Rev. Lett.* **1993**, *71*, 1087; i) D. Phelan, E. E. Rodriguez, J. Gao, Y. Bing, Z.-G. Ye, Q. Huang, J. Wen, G. Xu, C. Stock, M. Matsuura, *Phase Transitions* **2015**, *88*, 283.

[5] a) R. Cowley, S. Gvasaliya, S. Lushnikov, B. Roessli, G. Rotaru, *Adv. Phys.* **2011**, *60*, 229; b) A. A. Bokov, Z.-G. Ye, *J. Mater. Sci.* **2006**, *41*, 31.

[6] G. Xu, P. Gehring, C. Stock, K. Conlon, *Phase Transitions* **2006**, *79*, 135.

[7] a) W. S. Chang, M. Shanthi, K. K. Rajan, L. C. Lim, F. T. Wang, C. T. Tseng, C. S. Tu, P. Yang, H. O. Moser, *J. Appl. Phys.* **2007**, *101*, 124104; b) M. F. Wong, K. Zeng, *J. Am. Ceram. Soc.* **2011**, *94*, 1079.

[8] E. H. Kisi, J. S. Forrester, *J. Phys.: Condens. Matter* **2005**, *17*, L381.

[9] a) C. Stock, R. Birgeneau, S. Wakimoto, J. Gardner, W. Chen, Z.-G. Ye, G. Shirane, *Phys. Rev. B* **2004**, *69*, 094104; b) C. Stock, D. Ellis, I. Swainson, G. Xu, H. Hiraka, Z. Zhong, H. Luo, X. Zhao, D. Viehland, R. Birgeneau, *Phys. Rev. B* **2006**, *73*, 064107; c) J. Hill, T. Thurston, R. Erwin, M. Ramstad, R. Birgeneau, *Phys. Rev. Lett.* **1991**, *66*, 3281.

[10] P. Gao, H.-J. Liu, Y.-L. Huang, Y.-H. Chu, R. Ishikawa, B. Feng, Y. Jiang, N. Shibata, E.-G. Wang, Y. Ikuhara, *Nat. Commun.* **2016**, *7*, 11318.

[11] K. L. Brown, C. P. Stockdale, H. Luo, X. Zhao, J. Li, D. Viehland, G. Xu, P. M. Gehring, K. Ishida, A. Hillier, *J. Phys.: Condens. Matter* **2018**, *30*, 125703.

[12] X. Zhang, Q. Pan, D. Tian, W. Zhou, P. Chen, H. Zhang, B. Chu, *Phys. Rev. Lett.* **2018**, *121*, 057602.

[13] A. Biancoli, C. M. Fancher, J. L. Jones, D. Damjanovic, *Nat. Mater.* **2015**, *14*, 224.
[14] X. Zhang, T. J. Kennedy, E. V. Colla, M. B. Weissman, D. D. Viehland, *J. Appl. Phys.* **2018**, *124*, 234102.
[15] U. K. Bhaskar, N. Banerjee, A. Abdollahi, Z. Wang, D. G. Schlom, G. Rijnders, G. Catalan, *Nat. Nanotechnol.* **2016**, *11*, 263.
[16] K. Garrity, A. Kolpak, S. Ismail-Beigi, E. Altman, *Adv. Mater.* **2010**, *22*, 2969.
[17] a) M. Höfling, S. Steiner, A.-P. Hoang, I.-T. Seo, T. Frömling, *J. Mater. Chem. C* **2018**, *6*, 4769; b) M. Li, M. J. Pietrowski, R. A. De Souza, H. Zhang, I. M. Reaney, S. N. Cook, J. A. Kilner, D. C. Sinclair, *Nat. Mater.* **2014**, *13*, 31; c) M. Li, H. Zhang, S. N. Cook, L. Li, J. A. Kilner, I. M. Reaney, D. C. Sinclair, *Chem. Mater.* **2015**, *27*, 629.
[18] a) A. R. Paterson, H. Nagata, X. Tan, J. E. Daniels, M. Hinterstein, R. Ranjan, P. B. Groszewicz, W. Jo, J. L. Jones, *MRS Bull.* **2018**, *43*, 600; b) V. V. Shvartsman, D. C. Lupascu, *J. Am. Ceram. Soc.* **2012**, *95*, 1; c) J. Rödel, K. G. Webber, R. Dittmer, W. Jo, M. Kimura, D. Damjanovic, *J. Eur. Ceram. Soc.* **2015**, *35*, 1659; d) G. Esteves, C. M. Fancher, J. L. Jones, *J. Mater. Res.* **2015**, *30*, 340; e) D. Hou, C. Zhao, A. R. Paterson, S. Li, J. L. Jones, *J. Eur. Ceram. Soc.* **2018**, *38*, 971.
[19] W. Ge, C. P. Devreugd, D. Phelan, Q. Zhang, M. Ahart, J. Li, H. Luo, L. A. Boatner, D. Viehland, P. M. Gehring, *Phys. Rev. B* **2013**, *88*, 174115.
[20] A. Thompson, D. Vaughan, *X-Ray Data Booklet*, Lawrence Berkeley National Laboratory, Berkeley, CA **2001**.
[21] P. B. Groszewicz, M. Gröting, H. Breitzke, W. Jo, K. Albe, G. Buntkowsky, J. Rödel, *Sci. Rep.* **2016**, *6*, 31739.
[22] K. Conlon, H. Luo, D. Viehland, J. Li, T. Whan, J. Fox, C. Stock, G. Shirane, *Phys. Rev. B* **2004**, *70*, 172204.
[23] J. M. Gere, B. J. Goodno, *Mechanics of Materials*, Cengage Learning, Toronto **2008**.
[24] a) J. E. Daniels, W. Jo, J. Rödel, V. Honkimäki, J. L. Jones, *Acta Mater.* **2010**, *58*, 2103; b) J. E. Daniels, G. Picht, S. Kimber, K. G. Webber, *Appl. Phys. Lett.* **2013**, *103*, 122902.
[25] J. Oddershede, M. J. Hossain, J. E. Daniels, *Appl. Phys. Lett.* **2016**, *109*, 092901.
[26] a) M. Vögler, J. Daniels, K. Webber, J. Rödel, *Scr. Mater.* **2017**, *136*, 115; b) P. Kumar, K. Prashant, *Elements of Fracture Mechanics*, Tata McGraw-Hill Education, Delhi **2009**.
[27] a) M. Bobeth, N. Farag, A. A. Levin, D. C. Meyer, W. Pompe, A. E. Romanov, *J. Ceram. Soc. Jpn.* **2006**, *114*, 1029; b) J. Hanzig, M. Zschornak, E. Mehner, F. Hanzig, W. Münchgesang, T. Leisegang, H. Stöcker, D. C. Meyer, *J. Phys.: Condens. Matter* **2016**, *28*, 225001; c) B. Khanbabaee, E. Mehner, C. Richter, J. Hanzig, M. Zschornak, U. Pietsch, H. Stöcker, T. Leisegang, D. Meyer, S. Gorfman, *Appl. Phys. Lett.* **2016**, *109*, 222901; d) D. Meyer, A. Levin, S. Bayer, A. Gorbunov, W. Pompe, P. Paufler, *Appl. Phys. A* **2005**, *80*, 515.
[28] a) S. B. Mi, C. L. Jia, T. Heeg, O. Trithaveesak, J. Schubert, K. Urban, *J. Cryst. Growth* **2005**, *283*, 425; b) T. Zhao, F. Chen, H. Lu, G. Yang, Z. Chen, *J. Appl. Phys.* **2000**, *87*, 7442; c) C. L. Li, Z. H. Chen, Y. L. Zhou, D. F. Cui, *J. Phys.: Condens. Matter* **2001**, *13*, 5261.
[29] a) D. Marrocchelli, S. R. Bishop, H. L. Tuller, B. Yildiz, *Adv. Funct. Mater.* **2012**, *22*, 1958; b) D. Marrocchelli, N. H. Perry, S. R. Bishop, *Phys. Chem. Chem. Phys.* **2015**, *17*, 10028.
[30] Y. Imry, S.-k. Ma, *Phys. Rev. Lett.* **1975**, *35*, 1399.
[31] N. Kumar, E. A. Patterson, T. Frömling, E. P. Gorzkowski, P. Eschbach, I. Love, M. P. Müller, R. A. De Souza, J. Tucker, S. R. Reese, *J. Am. Ceram. Soc.* **2018**, *101*, 2376.
[32] D. M. Smyth, *The Defect Chemistry of Metal Oxides*, Oxford University Press, New York **2000**.
[33] a) S. Prasertpalichat, W. Schmidt, D. P. Cann, *J. Adv. Dielectr.* **2016**, *06*, 1650012; b) F. Yang, M. Li, L. Li, P. Wu, E. Pradal-Velázquez, D. Sinclair, *J. Mater. Chem. A* **2018**, *6*, 5243.
[34] X. Shi, N. Kumar, M. Hoffman, *J. Mater. Chem. C* **2018**, *6*, 12224.
[35] N. Kumar, E. A. Patterson, T. Frömling, E. P. Gorzkowski, P. Eschbach, I. Love, M. P. Müller, R. A. De Souza, J. Tucker, S. R. Reese, D. P. Cann, *J. Am. Ceram. Soc.* **2018**, *101*, 2376.
[36] R. D. Shannon, *Acta Crystallogr. A* **1976**, *32*, 751.
[37] a) J. E. Daniels, W. Jo, J. Rödel, J. L. Jones, *Appl. Phys. Lett.* **2009**, *95*, 032904; b) K. G. Webber, Y. Zhang, W. Jo, J. E. Daniels, J. Rödel, *J. Appl. Phys.* **2010**, *108*, 014101.
[38] J. E. Daniels, A. Pramanick, J. L. Jones, *IEEE Trans. Ultrason., Ferroelectr., Freq. Control* **2009**, *56*, 1539.
[39] J. P. Perdew, K. Burke, M. Ernzerhof, *Phys. Rev. Lett.* **1996**, *77*, 3865.
[40] a) G. Kresse, *Phys. Rev. B* **1996**, *54*, 11169; b) G. Kresse, D. Joubert, *Phys. Rev. B* **1999**, *59*, 1758.
[41] P. E. Blöchl, *Phys. Rev. B* **1994**, *50*, 17953.
[42] a) C. Cazorla, M. Stengel, *Phys. Rev. B* **2015**, *92*, 214108; b) C. Cazorla, O. Diéguez, J. Íñiguez, *Sci. Adv.* **2017**, *3*, e1700288.

